Amplified seasonal range in precipitation minus evaporation

Allan, R. P. ORCID: https://orcid.org/0000-0003-0264-9447 (2023) Amplified seasonal range in precipitation minus evaporation. Environmental Research Letters, 18 (9). 094004. ISSN 1748-9326 doi: https://doi.org/10.1088/1748-9326/acea36 Available at https://centaur.reading.ac.uk/112694/

ENVIRONMENTAL RESEARCH
LETTERS

LETTER • OPEN ACCESS

Amplified seasonal range in precipitation minus evaporation

To cite this article: Richard P Allan 2023 *Environ. Res. Lett.* **18** 094004

IOP Publishing Environ. Res. Lett. 18 (2023) 094004 https://doi.org/10.1088/1748-9326/acea36

ENVIRONMENTAL RESEARCH
LETTERS

LETTER

Amplified seasonal range in precipitation minus evaporation

Richard P Allan

Department of Meteorology/National Centre for Earth Observation, University of Reading, Reading, Berkshire, United Kingdom

E-mail: r.p.allan@reading.ac.uk

Keywords: climate, precipitation, water

Supplementary material for this article is available online

OPEN ACCESS

RECEIVED
6 June 2023

REVISED
6 July 2023

ACCEPTED FOR PUBLICATION
25 July 2023

PUBLISHED
10 August 2023

Abstract

Climate warming is intensifying the global water cycle, including the rate of fresh water flux between the atmosphere and the surface, determined by precipitation minus evaporation (P−E). Surpluses or deficits of fresh water impact societies and ecosystems, so it is important to monitor and understand how and why P−E patterns and their seasonal range are changing across the globe. Here, annual maximum and minimum P−E and their changes are diagnosed globally over land and ocean using observation-based datasets and CMIP6 climate model experiments covering 1950–2100. Seasonal minimum P−E is negative across much of the globe, apart from the Arctic, mid-latitude oceans and the tropical warm pool. In the global mean, P−E maximum increases and P−E minimum decreases by around 3%–4% per °C of global warming from 1995–2014 to 2080–2100 in the ensemble mean of an intermediate greenhouse gas emission scenario. Over land, there is less coherence across the 1960–2020 datasets, but an increase in the seasonal range in P−E emerges in future projections. Patterns of future changes in annual maximum and minimum P−E are qualitatively similar to present day trends with increases in maximum P−E in the equatorial belt and high-latitude regions and decreases in the subtropical subsidence zones. This adds confidence to future projections of a more variable and extreme water cycle but also highlights uncertainties in this response over land.

1. Introduction

Climate warming intensifies the global water cycle with greater flows of moisture, increased variability in space and time, and growing water-related risks to societies (Pendergrass *et al* 2017, Allan *et al* 2020, Douville *et al* 2021, 2022). While attention has focused on short-duration hourly to multi-day extremes (Fowler *et al* 2021, Seneviratne *et al* 2021), considerable impacts are also felt through seasonal and multi-annual events including seasonal flooding and droughts (e.g. Marsh *et al* 2013, Wainwright *et al* 2021) and their effects on vegetation (e.g. Alexander *et al* 2023).

A consequence of intensified moisture transport in warmer climates is the amplification of existing precipitation minus evaporation (P−E) patterns (Held and Soden 2006). This tendency is robust over the ocean where it enhances salinity patterns (Skliris *et al* 2014) but over land the situation is more complex (Greve *et al* 2014, Duan *et al* 2023, Zaitchik *et al* 2023); here, multi-annual P–E is positive, with a net flow of moisture from ocean to land that is known to increase on average with global warming (Byrne and O'Gorman 2018). However, the terrestrial response is further affected by changes in atmospheric circulation patterns, land surface feedback and vegetation responses to carbon dioxide, climate and land use change (Byrne and O'Gorman 2015, Berg *et al* 2016, Douville *et al* 2021, Liu *et al* 2023). Combined with the resulting greater warming over land than the ocean, these processes drive a decline in relative humidity (Byrne and O'Gorman 2016), the processes of which are uncertain, with discrepancies between observations, simulations and theoretical predictions (Simmons *et al* 2010, Chadwick *et al* 2013, Dunn *et al* 2017, Samset *et al* 2018, Allan *et al* 2020, 2022, Douville *et al* 2020).

The purpose of the present study is to investigate longer duration (monthly–seasonal) changes in freshwater fluxes diagnosed by P−E. Although not directly related to aridity, which also depends upon the capacity of the atmosphere to evaporate water (Roderick *et al* 2014, Greve and Seneviratne 2015, Scheff and Frierson 2015, Milly and Dunne 2016, Ficklin *et al* 2022, Duan *et al* 2023), P–E is nevertheless an important and fundamental diagnostic of the global climate system. Although multi-annual P−E is positive and balanced by runoff over land, this is not the case seasonally (Chou *et al* 2013, Kumar *et al* 2015) since after a wet period or season, water is evaporated and exported. This can explain a tendency for precipitation, P−E and water supply and demand to increase in wet parts of the atmospheric circulation and decrease in drier subsidence zones (Liu and Allan 2013, Schurer *et al* 2020, Ficklin *et al* 2022), symptomatic of a greater intensity of wet and dry events where and when they occur. Increased variability, including rapid swings between dry and wet conditions, is also considered to be a damaging consequence of a warming climate (Chen *et al* 2022, Chen and Wang 2022, Tan *et al* 2023).

Here, the objective is to investigate present and future changes in P−E (1950–2100) using observation-based datasets and climate model simulations, with a focus on the annual maximum and minimum. This isolates the wettest time of year whenever it occurs, such as the tropical wet season or a wet period linked to fluctuations in atmospheric circulation. Conversely, annual P−E minimum does not relate directly to the driest season or period over more arid land since P−E tends to zero after a lengthy dry spell as the soil moisture is depleted; instead, P−E minimum over land is symptomatic of the intensity at the onset of a dry period, which is also relevant for flash droughts (Pendergrass *et al* 2020, Black 2023, Yuan *et al* 2023).

2. Data and methods

Global satellite and rain gauge-based precipitation estimates are combined with evaporation from a global reanalysis and these are compared with direct and indirect estimates of P−E from the reanalysis and a range of climate model simulations. Although a larger range of observational products could be considered, it was decided to focus on widely used dataset combinations in the present study to evaluate robust climate responses.

2.1. Precipitation observations

Global Precipitation Climatology Project version 2.3 monthly 0.5 × 0.5° resolution combined satellite and rain gauge data (GPCPv2.3MON) is available for 1983–2020 (Huffman 2021). It uses a range of microwave, infrared and radar satellite products that are merged with surface rain gauge records from the Global Precipitation Climatology Centre (GPCC; Becker *et al* 2013) which is based on monthly estimates from synoptic weather reports at the Deutscher Wetterdienst, Germany, and at the Climate Prediction Center/National Oceanic and Atmospheric Administration, USA, and monthly precipitation totals extracted from CLIMAT bulletins. The period January 1983–December 1991 lacks the Goddard profiling algorithm and so is considered less reliable. The 0.25 × 0.25° GPCC Full Data Monthly Product Version 2022 land data is also considered independently for the period 1960–2020.

2.2. Reanalysis data

The fifth-generation European Centre for Medium-range Weather Forecasts (ECMWF) global reanalysis (ERA5; Hersbach *et al* 2020) combines observations with a high-resolution atmosphere modeling system via four-dimensional-variational (4D-Var) data assimilation. Extensive conventional and satellite observations of surface and tropospheric temperature and humidity are assimilated, including Special Sensor Microwave/Imager (SSM/I), Atmospheric InfraRed Sounder (AIRS) and High-resolution Infrared Radiation Sounder (HIRS) radiance data that are also used to construct the GPCP dataset employed in the present study. ERA5 provides a consistent hourly record of the atmosphere, land and ocean surface since 1950 using a ∼31 km horizontal grid and 137 levels in the vertical. Monthly means of daily means covering the period 1960–2021 are considered. Data on a 0.25 × 0.25 latitude-longitude grid are extracted, considering total precipitation, surface evaporation and vertically integrated moisture divergence.

2.3. Climate models

An ensemble of climate-model simulations contributing to the CMIP6 *historical, amip* and *ssp2-4.5* experiments were selected (table 1) based on the availability of diagnostics. Although the full set of CMIP6 models is not considered, doing so would still not ensure that the full range of uncertainty is captured and the set of 18 models is deemed a suitable number to sufficiently represent internal variability as well as model structural uncertainty (e.g. Allan *et al* 2022).

The *historical* experiments represent realistic changes in radiative forcings that drive coupled versions of the climate models over the period 1850–2014 (the 1950–2014 subset is extracted). The *ssp2-4.5* experiment represents an intermediate greenhouse gas emission future scenario that stabilizes radiative forcing at about 4.5 Wm^{-2} by 2100 (Thomson *et al* 2011). One ensemble member per model is chosen, as follows: r1i1p1f1 apart from CNRM/GISS/UKESM models (r1i1p1f2) and HadGEM3 (r1i1p1f3), which

Table 1. Global and land mean P−E for 3 month maximum, minimum and annual mean (land) across models and experiments (*historical* and *amip*) and observation-based estimates (1995−2013).

	Global				Global land					
P–E (mm d^{-1})	Maximum		Minimum		MEAN		MAX		MIN	
Model/experiment	*hist*	*amip*	*hist*	*amip*	*hist*	*amip*	*hist*	*amip*	*hist*	*amip*
ACCESS-ESM1-5[A]	2.65	2.48	−2.05	−1.98	1.16	1.36	4.41	4.76	−1.09	−1.09
BCC-CSM2-MR[B]	2.50	2.41	−1.99	−1.95	1.17	1.32	4.20	4.67	−0.76	−0.91
BCC-ESM1[b]	2.38	2.36	−1.90	−1.87	1.46	1.26	4.87	4.58	−0.90	−0.97
CanESM5[a]	2.46	2.34	−2.00	−1.95	0.97	1.16	4.44	4.82	−1.53	−1.51
CESM2[C]	2.47	2.22	−2.00	−1.87	1.23	1.54	4.72	5.04	−1.22	−1.03
CESM2-WACCM[W]	2.37	2.22	−1.95	−1.87	1.24	1.51	4.67	5.02	−1.19	−1.06
CMCC-CM2-SR5[c]	2.32	2.14	−1.93	−1.86	1.22	1.45	4.15	4.42	−0.93	−0.78
CNRM-CM6-1[N]	2.52	2.40	−2.11	−2.04	0.93	0.87	3.82	3.33	−1.19	−1.00
CNRM-ESM2-1[n]	2.52	2.41	−2.13	−2.04	0.95	0.87	3.89	3.39	−1.25	−1.05
GFDL-ESM4[G]	2.49	2.41	−2.02	−1.97	0.93	1.01	4.42	4.31	−1.53	−1.41
GISS-E2-1-G[g]	2.48	2.51	−2.00	−2.01	0.66	0.54	3.16	3.01	−1.12	−1.16
HadGEM3-GC31-LL[H]	2.56	2.49	−2.05	−2.03	0.93	0.88	3.69	3.43	−1.05	−1.00
INM-CM5-0[I]	2.23	2.31	−1.85	−1.90	1.06	0.99	3.65	3.49	−0.83	−0.84
IPSL-CM6A-LR[i]	2.40	2.27	−2.03	−1.96	1.38	1.63	4.31	4.57	−0.84	−0.67
MIROC6[M]	2.48	2.57	−2.04	−2.10	1.13	0.97	4.70	4.11	−1.45	−1.32
MRI-ESM2-0[m]	2.63	2.44	−2.15	−2.06	1.04	1.23	4.24	4.50	−1.45	−1.37
NorESM2-LM[o]	2.39	2.29	−1.94	−1.91	0.95	1.22	4.26	4.52	−1.40	−1.28
UKESM1-0-LL[U]	2.53	2.47	−2.05	−2.03	0.94	0.93	3.73	3.55	−1.13	−1.04
Ensemble mean	2.47	2.37	−2.01	−1.97	1.08	1.15	4.18	4.20	−1.16	−1.08
GPCP/ERA5-adj[P,E]		2.27		−1.88		1.02		3.77		−0.97
ERA5-adj[E]		2.17		−1.81		1.13		3.78		−0.81
ERA5-MDiv-adj[E]		2.18		−1.82		1.08		3.84		−1.00

[A] Ziehn *et al* (2020); [B,b]Wu *et al* (2019, 2020); [a]Swart *et al* (2019); [C,W]Gettelman *et al* (2019); [c]Scoccimarro *et al* (2022); [N]Voldoire *et al* (2019); [n]Séférian *et al* (2019); [G]Zhao *et al* (2018); [g]Schmidt *et al* (2014); [H]Andrews *et al* (2020); [I]Song *et al* (2021); [i]Boucher *et al* (2020); [M]Tatebe *et al* (2019); [m]Yukimoto *et al* (2019); [o]Seland *et al* (2020); [U]Swaminathan *et al* (2022); [P]Huffman (2021); [E]Hersbach *et al* (2020).

accounts for slight adjustments to the forcings required to produce the required CMIP6 simulations and CESM2 (r11i1p1f1 since r1i1p1f1 was not available in all simulations at the time). Although analyzing more scenarios would provide additional information on plausible future projections, *ssp2-4.5* was chosen as a focus since it covers a broad range of global warming by the end of the twenty-first century (∼2.3 ± 1 °C relative to present) due to varying climate sensitivity and ocean heat uptake across models and does not include very high and very low emission scenarios that may be less relevant baselines for policy making (e.g. Hausfather and Peters 2020).

2.4. Methodology

P−E was computed for climate model simulations and ERA5 as well as for observation-based estimates: GPCP precipitation minus ERA5 evaporation; GPCC precipitation over land and ERA5 precipitation over ocean combined with ERA5 evaporation. In addition to direct estimates of P−E from ERA5, an independent ERA5 estimate was constructed (see also supplementary information) from the residual of horizontal moisture flux divergence ($\nabla \cdot \mathbf{F}$) and changes in column integrated water vapor (ΔW) between midnight at the beginning of the first day and end of the last day of the month (a minor term):

$$P - E = -\nabla \cdot \mathbf{F} - \Delta W. \quad (1)$$

Based on scrutiny of the observation-based datasets, to account for unrealistic global imbalance in the water budget and artificial drifts over time, a relative (%) adjustment in ocean evaporation was applied to ensure global annual mean P−E = 0 (see supplementary information; figures S1 and S2). While moisture imbalances affected older generations of models (Liepert and Previdi 2012), this is not expected to affect CMIP6 and the *amip* set of simulations is able to close the global water budget such that the global mean $P - E \sim 0$ (figure S1).

Annual monthly and 3 month maximum and minimum P−E were next computed over the range of simulated and observed records for each gridpoint. The timing of maximum and minimum is allowed to vary across observations, models and year, thereby focusing in on the wettest or driest times of the year, in terms of P–E, whenever they occur. The month or 3 month of maximum or minimum were retained (the mode is displayed for climatological averages in figure S6). Although there is some

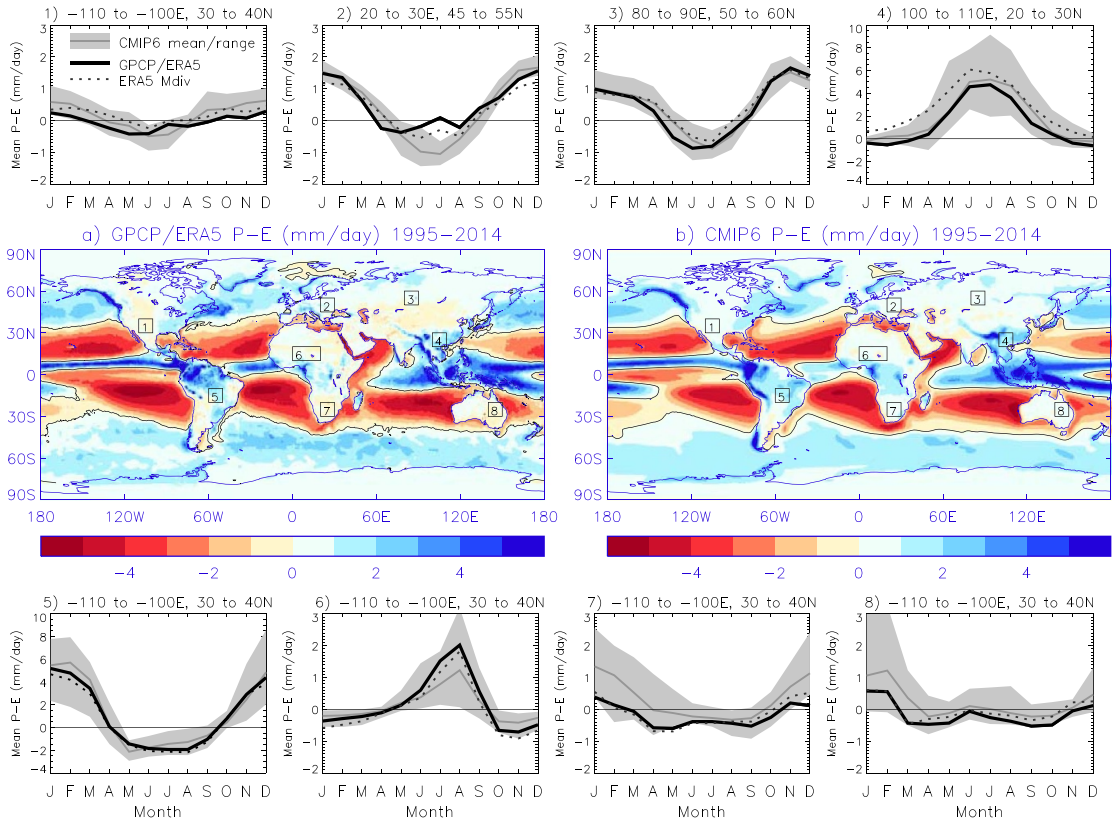

Figure 1. Climatological multi-annual mean precipitation minus evaporation (1995–2014) for (a) GPCP precipitation minus ERA5 evaporation and (b) CMIP6 ensemble mean. Seasonal cycles corresponding to numbered regions in the main panels are shown for CMIP6 (including model range), GPCP/ERA5 and ERA5 moisture divergence minus atmospheric storage.

variation in timing across models and experiments, the broad structure of timing is generally consistent (not shown). Annual 3 month maximum and minimum run from January–March to December–February, which explains why climatological estimates effectively span one fewer year at the end of the record compared with 1 month annual maximum (e.g. 1995–2013 compared to 1995–2014).

3. Results

3.1. Seasonal climatology

Figure 1 illustrates that the CMIP6 ensemble is able to represent the broad characteristics of observed P−E global climatology and seasonal cycles from eight example land locations (see also figures S2 and S3). Moist biases over 0–10 °S oceans highlight continued issues with an unrealistically pronounced double inter-tropical convergence zone (ITCZ), while a dry bias in the tropical warm pool region also remains in CMIP6, even when observed sea surface temperatures (SST) are prescribed (*amip*); model biases are comparable in magnitude to projected century time-scale future changes in P−E (figures S2(b)–(d)). Also shown are seasonal cycles in P−E derived from the moisture divergence fields, which are comparable to the GPCP/ERA5 and simulated estimates (figure 1), though ERA5 estimates produce more positive P−E ($\sim +1$ mm d^{-1}) over the east Pacific ITCZ (figures S2(e) and (f)) and south Asia (figure 1(4)). The CMIP6 models also simulate more negative P−E (~ -1 mm d^{-1}) in the eastern Europe region during summer (figure 1(2)).

Climatological annual 3 month maximum and minimum P−E (figure 2; modal timings in figure S6) also display similar regional structure to mean P–E fields but with positive P−E predominating for seasonal maximum in all but the most evaporative ocean regions (figure 2(a)) while P−E is negative for all but the highest latitudes and tropical warm pool center for the seasonal minimum (figure 2(c)). The annual monthly maximum and minimum P−E is similar in spatial pattern but around 1.5–2 mm d^{-1} more positive for maximum and 0.5–1 mm d^{-1} more negative for minimum (figure S4; tables 1 and S1). Over land, the seasonal maximum P−E is almost exclusively positive, while the seasonal minimum is negative. This is important since it shows that an amplification of P−E patterns can decrease negative P−E over land during dry seasons or multi-month events, thereby leading to an amplification of wet and dry events, as previously implied (Chou *et al* 2013, Kumar *et al* 2015).

The observed zonal structure in maximum, mean and minimum P−E (figures 2(e)–(g)) is well captured

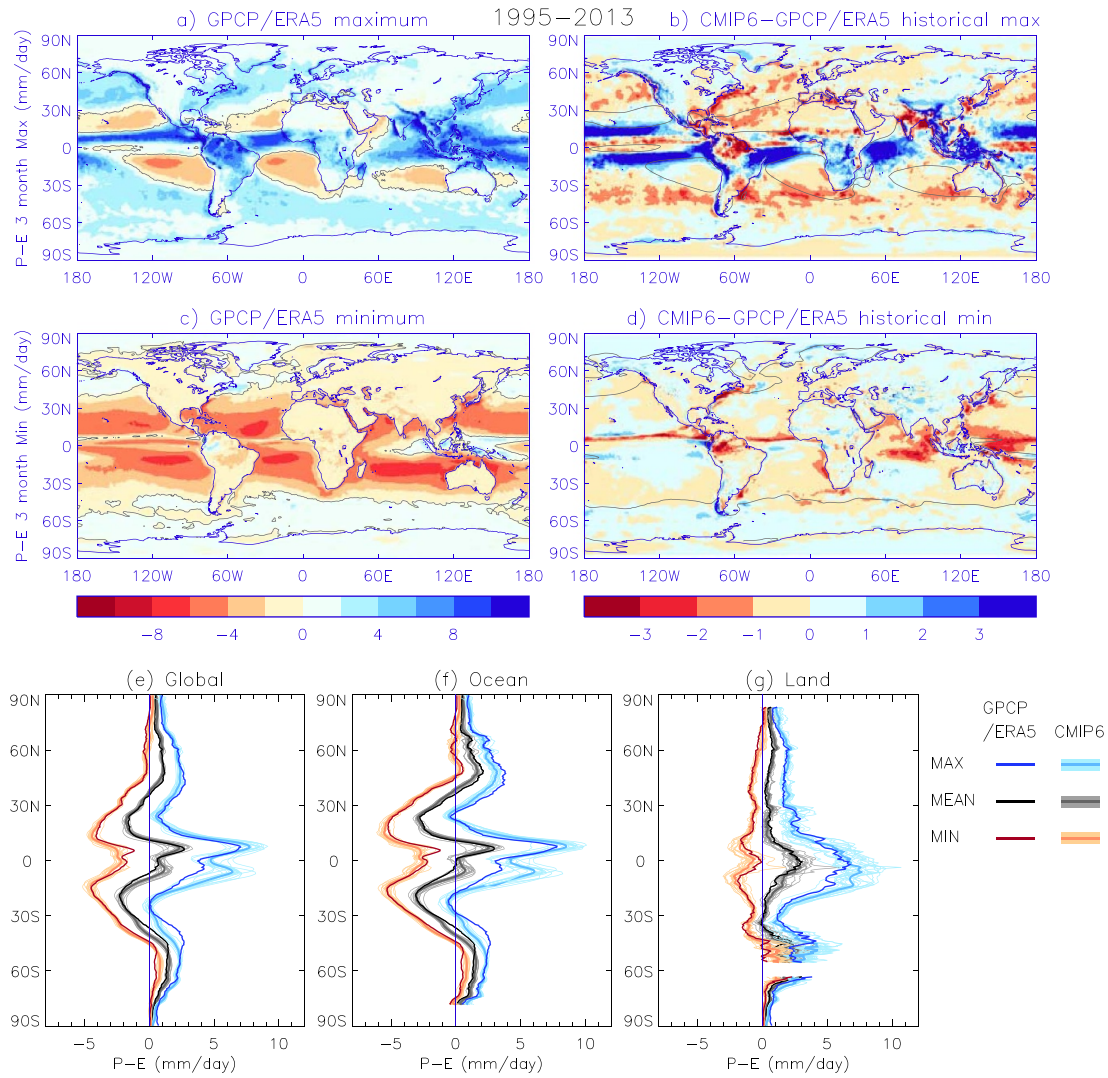

Figure 2. Climatological 3 month annual maximum (a)–(b) and minimum (c)–(d) P−E for GPCP/ERA5 and CMIP6 ensemble minus GPCP/ERA5 difference and their zonal means including also mean P−E (e) and over (f) ocean and (g) land for 1995–2013.

by CMIP6 simulations but with a notable overestimate in the annual maximum P−E around 0–10 °S (which is less prominent for the CESM and MIROC6 models, not shown). An apparent model underestimate over the ocean around 30–40 °S (figure 2(b)) is expected to be an artifact of GPCP observations since a consistent discrepancy is identified for *amip* simulations and both ERA5 estimates (figures S5 and S7).

These characteristics are similar for annual monthly maximum/minimum P−E (figure S4) but the 0–10 °S bias is diminished in *amip* simulations suggesting a role of SST biases here (figure S5). A less prominent overestimate in CMIP6 P−E 0–10 °N over the east Pacific and Atlantic is also apparent in P−E minimum (figure 2(d)), which also applies to the periphery of the tropical warm pool region (biases are smaller in CESM and MIROC6 models, not shown). Global mean P−E maximum and minimum are generally of larger magnitude by ∼10% in CMIP6 *historical* and *amip* simulations than observations (table 1).

3.2. Current trends

Trends in mean, maximum and minimum P−E 1983–2019 (figure 3) display some similarity between observed and simulated estimates, particularly in the zonal mean (right) though with larger magnitude observed regional changes. Increases in 0–10 °N P−E and decreases around 0–10 °S (most pronounced in the eastern Pacific and western Atlantic) may reflect the multi-decadal northward movement of the ITCZ, in part related to greenhouse gas forcing (Dong and Sutton 2015). Negative P−E trends simulated over the subtropical ocean and positive trends in the (northern) equatorial belt and higher latitudes show limited regions of significance but are consistent with an amplification in ocean salinity patterns, also found to be driven by greenhouse gas forcing (Skliris *et al* 2016). These changes are more pronounced for

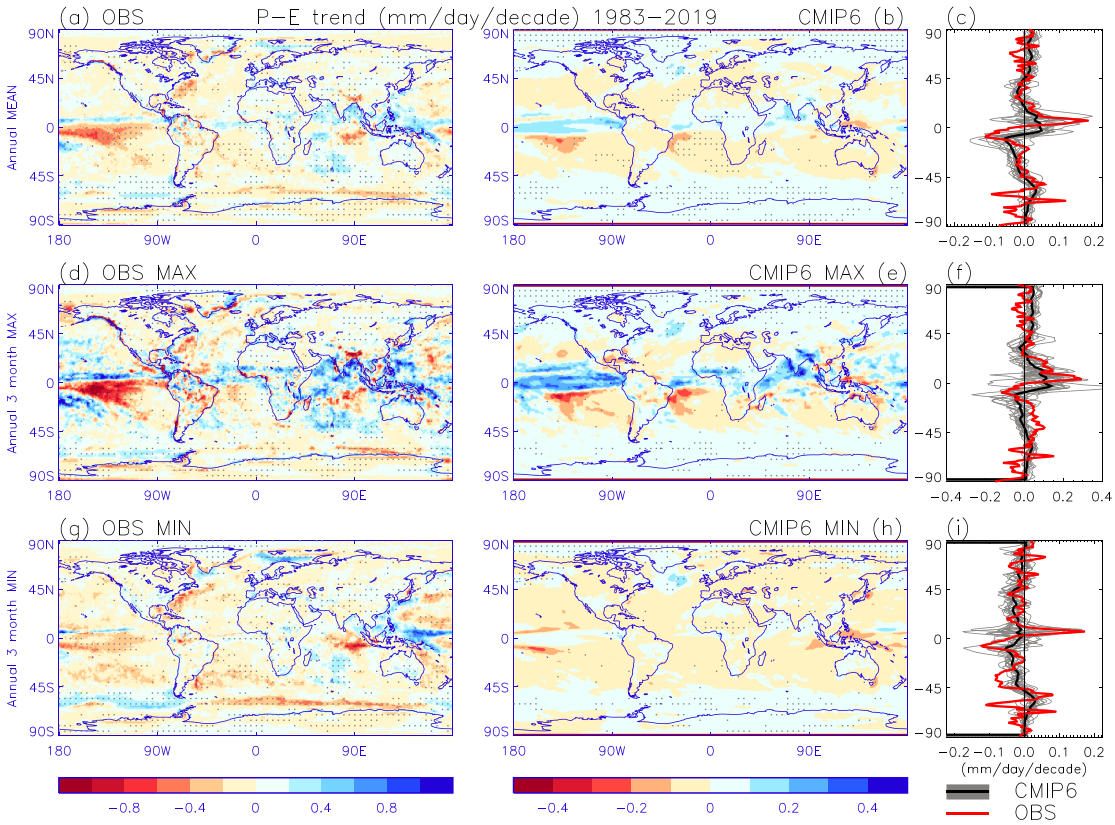

Figure 3. Trends in (a)–(c) annual mean and 3 month (d)–(f) maximum and (g)–(i) minimum P−E 1983–2019 in GPCP/ERA5 observations (left), CMIP6 *historical* and *ssp2-4.5* simulations (middle, note smaller colour bar range) and zonal global mean (right). Stippling denotes a significant linear trend at the 90% confidence level in observations and for at least four models.

annual maximum P−E (figures 3 and S10(d)–(f)) though are generally weakly negative for annual minimum P−E apart from in polar regions (figures 3 and S10(g)–(i)). Simulated decreases in minimum P−E on the periphery of the Pacific ITCZ may reflect a narrowing of the tropical rain belt (Byrne *et al* 2018, Su *et al* 2020). This tightening is not noticeable in the observations, which display a more general global decrease in 3 month minimum P−E (figure 3(g)), even more so when considering 1 month minimum (figure S10(g)).

The global trend patterns are similar for ERA5 estimates (though more pronounced in the tropics; figure S9) and also apply for a shorter time period (1983–2013) including for the *amip* simulations (figure S8), suggesting that unforced internal variability is not dominating; differences in the spatial structure evident in the tropical warm pool and decreases in the northern tropical east Pacific may, however, reflect the phases of the El Niño Southern Oscillation and global teleconnection patterns (e.g. Vázquez *et al* 2022) that depend on the chosen time period. These signals of unforced variability are essentially removed in the multi-model averaging of the CMIP6 *historical* and *ssp2-4.5* coupled simulations.

The tendency for annual maximum P−E to increase over time and for the minimum to decrease is apparent for all observation-based estimates and model simulations (figures 4(a) and (b)) but with substantial year-to-year variation that is generally anticorrelated between annual minimum and maximum time-series (e.g. the 1998 El Niño event shows elevated P−E maximum $\sim$+0.2 mm d^{-1} and around 0.1 mm d^{-1} lower (more negative) P–E minimum. The global trends are dominated by the oceans (figures 4(f)–(h)), while agreement among datasets and trends is less coherent over the global and tropical land (figures 4(c)–(e) and S13), particularly for P−E minimum, which declines in ERA5 but increases in the ERA5 indirect moisture divergence estimate (figure 4(e)). The discrepancy between ERA5 estimates is particularly pronounced for P−E minimum before 1980 (figure 4(b)); the minimum may therefore be more sensitive to changes in the observing system, with limited satellite coverage of tropospheric water vapour before this time (Hersbach *et al* 2020). However, differences with GPCC observations over land (figures 4(d) and (e)) are apparent before the late 1980s, coinciding with the period prior to the introduction of the assimilation of SSM/I microwave water vapour data in July 1987, with ERA5 direct P−E overestimating by up to 0.1 mm d^{-1} in the mean and the moisture divergence estimates underestimating P−E minimum by up to 0.1 mm d^{-1}. Good agreement across datasets after the 1980s suggests

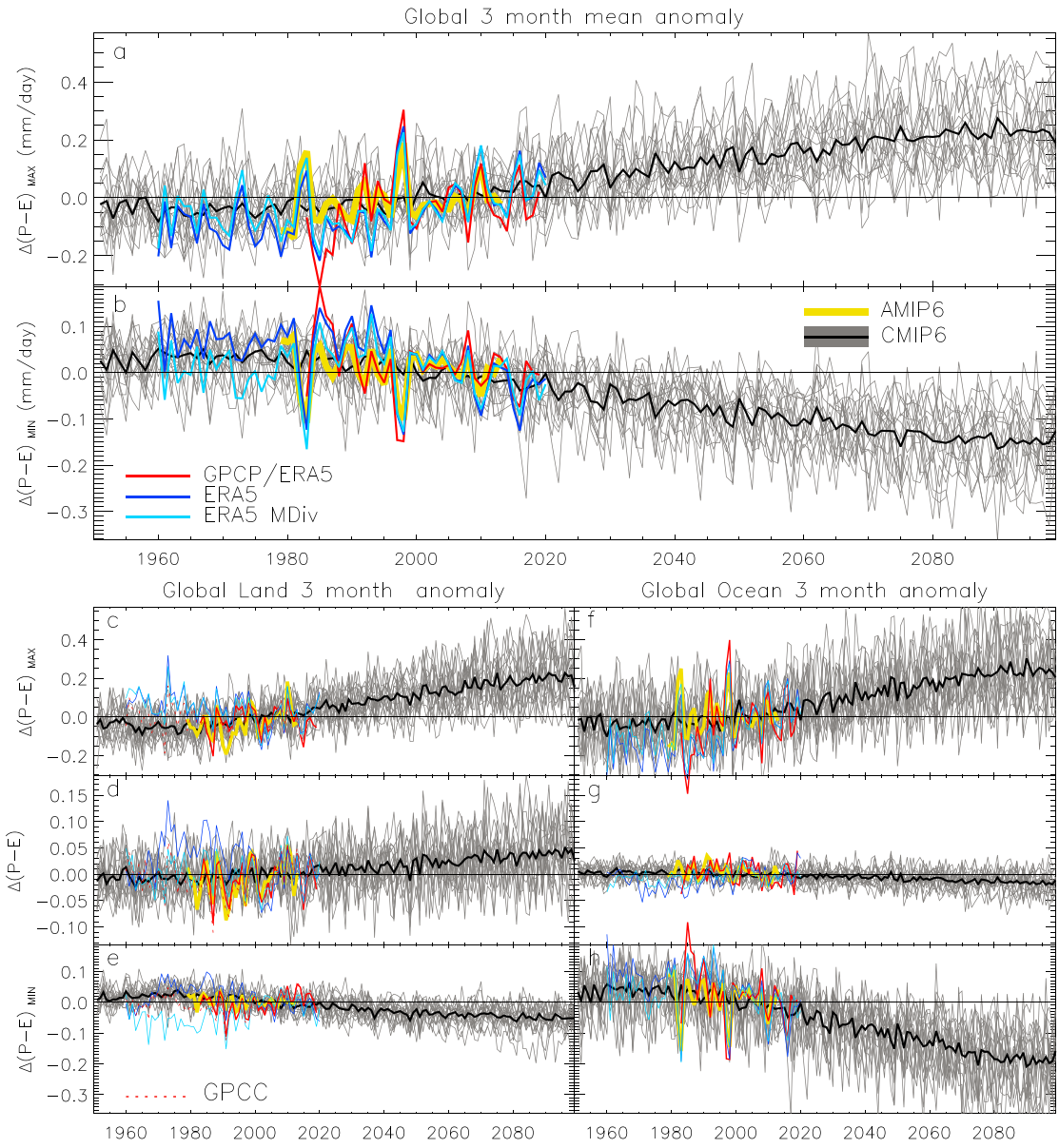

Figure 4. Global mean 3 month (a) maximum and (b) minimum P−E changes and for maximum, mean and minimum changes for global land (c)–(e) and global ocean (f)–(h). Individual *historical* and *ssp2-4.5* simulations (grey) and their ensemble mean (black) and *amip* ensemble mean (yellow) are compared with observational estimates from GPCP-ERA5, ERA5, ERA5 moisture divergence (MDiv) and over land only GPCC gauge records.

that this recent period is more robust in determining hydroclimatic changes.

For mean and maximum P−E over global land, substantial interannual variability is captured by the GPCP (and GPCC gauge-only) records, the *amip* simulations and ERA5 moisture divergence estimate as well as ERA5 P−E after the 1990s; this is primarily driven by unforced variability and so is absent in the *historical* simulation ensemble mean. A peak in 2010/11 P−E is associated with wet La Niña conditions over northern South America and Australia and replenishment of water in these regions and southeast Asia following the comparatively dry 2009/10 El Niño; this temporary additional terrestrial water storage resulted in a noticeable drop in sea level (Boening *et al* 2012). In contrast, a decline in mean and maximum P−E up to the El Niño of 2015/16 is associated with a drop in terrestrial water storage over Brazil and southern Africa (Blunden and Arndt 2016). Annual 1 month maximum and minimum P−E changes are qualitatively similar, with one notable exception: the GPCP/ERA5 estimate displays large decreases in P−E maximum and increases in the minimum before 2000 over the ocean, suggesting inhomogeneity in the satellite dataset estimates of low monthly rainfall totals that is not apparent when averaging over a seasonal time-scale (figures S10 and S14). Therefore, the observational period since 2000 is expected to be more robust for inferring hydroclimatic changes than the earlier period.

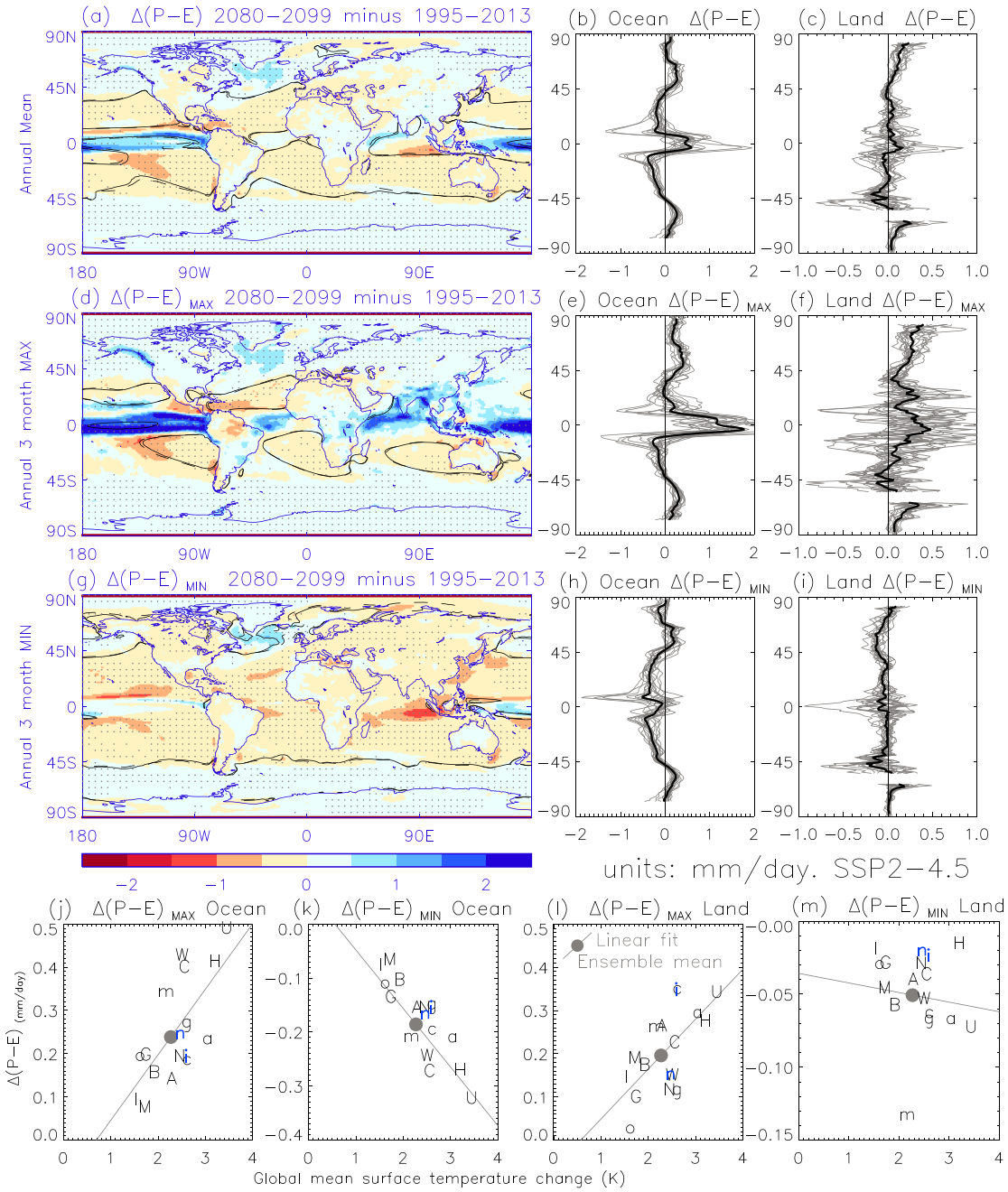

Figure 5. Projected P−E changes (2080–2100 minus 1995–2013) for (a)–(c) annual mean, (d)–(f) annual 3 month maximum and (g)–(i) annual 3 month minimum globally (left) and for zonal means over ocean (centre) and land (right). Stippling denotes 80% of models agree on the sign of change. Contours denote P−E = 0 over the ocean. Scatter plots show changes in global ocean or global land mean P−E annual 3 month maximum or minimum with global mean surface air temperature change for each model (j)–(m); letters as in table 1.

3.3. Future projections

Present day trends in P−E annual minimum and maximum continue across the twenty-first century in *ssp2-4.5* projections, with changes for 2080–2100 minus 1995–2013 as large in magnitude as $+0.44$ mm d^{-1} for maximum and -0.26 mm d^{-1} for minimum (HadGEM3) in the global mean (figures 4(a), (b) and table 2); these trends also begin to emerge over the global land (figures 4(c)–(e)), in contrast to the present day changes. Mean P−E increases over global land by $\sim$0.04 mm d^{-1} in the ensemble mean (table 2), reflecting the increase in moisture fluxes from ocean to land (Gimeno *et al* 2020); a corresponding smaller magnitude decline in global ocean mean P−E reflects the larger ocean area such that global P−E $\sim$0.

Future projections in P−E (figure 5(a)) generally show an amplification of existing P−E (figure 1(b)) which is dominated by the oceans (figures 2(f) and 5(b)) with less coherent changes evident over land (figure 5(c)), consistent with past studies (e.g. Held and Soden 2006, Greve and Seneviratne 2015). More general increases in annual maximum

Table 2. Global, ocean and land projected change (2080–2099 *ssp*2-4.5 minus 1995–2013 *historical*) in mean P−E for 3 month maximum, minimum and annual mean and global mean surface temperature change (ΔT) across models.

Δ(P–E) (mm d^{-1})	Global		Ocean			Land			ΔT (K)
Model	MAX	MIN	MAX	MEAN	MIN	MAX	MEAN	MIN	Global
ACCESS-ESM1-5	0.16	−0.13	0.13	−0.02	−0.16	0.25	0.06	−0.04	2.2
BCC-CSM2-MR	0.15	−0.10	0.14	−0.01	−0.11	0.16	0.02	−0.06	1.8
CanESM5	0.24	−0.18	0.22	−0.03	−0.22	0.28	0.07	−0.07	2.9
CESM2	0.34	−0.21	0.39	−0.02	−0.28	0.21	0.04	−0.04	2.4
CESM2-WACCM	0.34	−0.20	0.42	−0.00	−0.25	0.14	0.00	−0.06	2.4
CMCC-CM2-SR5	0.22	−0.16	0.17	−0.03	−0.20	0.34	0.09	−0.07	2.5
CNRM-CM6-1	0.16	−0.13	0.18	−0.01	−0.17	0.10	0.03	−0.03	2.3
CNRM-ESM2-1	0.21	−0.13	0.24	−0.01	−0.18	0.14	0.03	−0.02	2.3
GFDL-ESM4	0.16	−0.11	0.19	−0.00	−0.15	0.09	0.01	−0.03	1.6
GISS-E2-1-G	0.22	−0.13	0.26	0.00	−0.16	0.11	−0.00	−0.07	2.4
HadGEM3-GC31-LL	0.36	−0.21	0.40	−0.02	−0.28	0.26	0.06	−0.02	3.1
INM-CM5-0	0.10	−0.07	0.08	−0.01	−0.09	0.13	0.04	−0.02	1.5
IPSL-CM6A-LR	0.22	−0.13	0.18	−0.04	−0.17	0.33	0.10	−0.03	2.5
MIROC6	0.10	−0.07	0.06	−0.02	−0.08	0.18	0.04	−0.05	1.6
MRI-ESM2-0	0.31	−0.19	0.33	−0.01	−0.22	0.25	0.03	−0.14	2.0
NorESM2-LM	0.14	−0.09	0.18	0.01	−0.12	0.02	−0.03	−0.03	1.5
UKESM1-0-LL	0.44	−0.26	0.48	−0.02	−0.33	0.33	0.06	−0.08	3.3
Ensemble mean	0.23	−0.15	0.24	−0.02	−0.19	0.20	0.04	−0.05	2.3

P−E (figure 5(d)) and decreases in minimum P−E (figure 5(g)) are evident. There is an increase in maximum P−E over land in the CMIP6 ensemble mean at all latitudes, apart from 40 to 50 °S with robust increases across all models over high-latitude land (figure 5(f)). Decreases in annual minimum P−E over land are only robust over northern North America and Eurasia (0–0.3 mm d^{-1} more negative P−E around 40–70 °N; figure 5(i)). There is a general decrease in P−E minimum (more negative) over the ocean, particularly in the subtropics, but there are weak increases over the Southern Ocean and Antarctica and in the north Atlantic/Greenland/west Arctic region. There is an amplification in annual 3 month maximum minus minimum P−E range over most (86%) of the globe (figure S17); the magnitude change is dominated by increases in maximum over tropical wet regions, while a decrease in P−E range occurs in subtropical ocean regions of negative mean P−E but also over land regions subject to long-term drying such as parts of the Amazon, southern Africa, central Australia and the southwest USA. However, percentage changes in P−E range are generally larger over land (figures S17(e) and (f)), where mean P−E is smaller in magnitude than the ocean, and increases in P−E range greater than 20% occur over high-latitude regions including Siberia and Canada, as well as the equatorial Pacific (figure S17(d)).

It is noteworthy that the spatial patterns of future changes in annual maximum and minimum P−E (figures 5(d) and (g)) show qualitative similarity to present day trends (figures 3(e) and (h)) with increases in maximum P−E in the equatorial belt and decreases in the subtropical subsidence zones. Contraction and intensification of the ITCZ is an expected consequence of global warming (Byrne *et al* 2018, Su *et al* 2020) and this may be evident as bands of stronger decreases in P−E minimum over the east Pacific in recent trends (figure 3(h)) and future projections (figure 5(g)). Similarity in water cycle trends in the present day and future changes in dry season intensity have previously been documented across Brazil and southern Africa (e.g. Wainwright *et al* 2022) and attributed in part to greater warming over land than ocean, yet similar signals are not evident in P−E minimum.

Models simulating greater warming produce a larger amplification of global ocean or land mean P−E (figures 5(j)–(m)) and its seasonal range (figures S17(e) and (f)) with more positive maximum and more negative minimum as expected from thermodynamic arguments (Held and Soden 2006). For example, the UKESM produces the largest magnitude warming and P−E changes; water cycle changes across warming levels are discussed further by Swaminathan *et al* (2022) who identify drying in the Amazon and heavier Indian monsoons. Over land, although there is a clear increase in P−E maximum with warming across models, there is a less coherent decrease in P−E minimum with warming and the MRI-ESM2 model is an outlier. The strong decline in P−E minimum relative to the warming level may be linked to a previously identified hydrological response over land: in the 4xCO2 experiment the MRI-ESM2 model displayed a larger rapid increase in P in response to radiative forcing but a slower (compared to the IPSL-CM6A-LR model)

increase in P with the resulting multi decadal warming (Allan *et al* 2020). The MRI-ESM2 model historical simulation produces one of the largest magnitude global maximum ($+2.6$ mm d^{-1}) and minimum (-2.15 mm d^{-1}) P−E change that is also the case for the minimum P−E over global land (-1.45 mm d^{-1}; table 1); this distinct behaviour and less coherent response of land P−E seasonality to warming merits further analysis.

4. Conclusions

Precipitation minus evaporation determines the rate of input or loss of fresh water at the surface and is a fundamental diagnostic of climate change, playing a central role in the intensification of the water cycle with global warming. Despite a focus on daily and subseasonal weather extremes in relation to climate change (Seneviratne *et al* 2021), longer time-scale seasonal extremes are also important for impacts on societies (e.g. Marsh *et al* 2013, Wainwright *et al* 2021, Douville *et al* 2022). This can be particularly acute for rapid transitions between dry and wet conditions (Chen *et al* 2022, Chen and Wang 2022, Black 2023, Tan *et al* 2023). Analysis of changes in annual maximum and minimum P−E are therefore informative in assessing emerging signals of climate change and their regional manifestation, particularly in relation to wet seasons and periods as well as the onset of dry seasons and periods. This motivated the analysis of changes in annual mean, maximum and minimum P−E, which were assessed globally over the period 1950–2100 in observation-based datasets and climate model simulations. The main conclusions are:

(1) Maximum P−E is positive globally apart from subtropical ocean subsidence regions. Climate model *historical* simulations overestimate maximum P−E by around 3 mm d^{-1} over the 0–10 °S latitudes compared to GPCP/ERA5, particularly over the oceans but also in the equatorial north equatorial Pacific. These biases are less apparent in the zonal mean for *amip* simulations applying observed sea surface temperatures. GPCP/ERA5 produces higher P−E maximum over the ocean around 30–50 °S than *historical* and *amip* simulations, but also relative to the ERA5 estimates suggesting it may be an artifact of GPCP observations.

(2) Although multiannual P−E is positive over land, balancing runoff and river discharge, the onset of dry seasons or periods is associated with negative P−E. Seasonal minimum P−E is predominantly negative globally apart from high-latitude oceans and, for 3 month minimum only, small areas of the tropics, such as the tropical warm pool. Amplification of P−E patterns are therefore physically linked with stronger seasonality in water availability.

(3) Current changes in P−E show increases in annual maximum around 0–10 °N of up to 0.3 mm d^{-1} over the period 1983-2019, consistent with a northward movement of the tropical rain belt associated with greenhouse gas forcing and to a lesser extent changes in aerosol (e.g. Dong and Sutton 2015, Hirasawa *et al* 2022). An observed P−E decline in the tropical east Pacific is stronger than in *historical* simulations but represented by *amip*, and linked to weaker warming in this region than simulated by coupled models since 1979 (Dong *et al* 2021, Andrews *et al* 2022). Trends in P−E minimum are generally negative over the oceans but not statistically significant.

(4) All datasets display an increase in global average P−E maximum and decrease in P−E minimum since the 1980s that is dominated by the oceans and continues across the twenty-first century. Global P−E maximum increases by 0.23 mm d^{-1} (∼4% per °C global warming) and P−E minimum decreases by -0.15 mm d^{-1} (∼3%/°C) from 1995–2014 to 2080–2100 in the climate model ensemble mean. Climate models that simulate more warming also simulate stronger amplification in P−E seasonality (e.g. UKESM1 warms by 3.3 °C with $+0.44$ mm d^{-1} increase in maximum and -0.26 mm d^{-1} decrease in minimum P−E globally).

(5) Amplification in annual maximum and minimum P–E is dominated by the ocean in the present day with less coherence across datasets over land in recent decades. However, this amplification also emerges over land in future projections (ensemble mean P−E maximum increase of 0.2 mm d^{-1} and P–E minimum decrease of -0.05 mm d^{-1} from 1995–2014 to 2080–2100).

(6) Future changes in annual maximum and minimum P−E show qualitatively similar spatial patterns to present day trends, with increases in maximum P−E in the equatorial belt and high-latitude regions, but decreases in the subtropical subsidence zones. Annual minimum P−E decreases over much of the global ocean equatorwards of 45° apart from the equatorial band and there are also coherent decreases up to -0.3 mm d^{-1} over northern mid–high-latitude land (e.g. northern Eurasia and Canada). However, regional signals of dry season intensification over South America and southern Africa (Wainwright *et al* 2022) are not apparent in the present study, highlighting how hydroclimatic diagnostics are distinctly related across contrasting impacts.

(7) There is a less coherent relationship between decreases in annual minimum P−E and global warming for land with the MRI-ESM2 model exhibiting the largest sensitivity (-0.14 mm d^{-1} for 2 °C global warming, equivalent to a change of

5%/°C) that may be linked with a muted hydrological response to warming over land in this model based on results from previous idealized experiments (Allan *et al* 2020).

The increases in maximum and decreases in minimum annual P−E identified over land in the present study will intensify wet and dry periods and seasons that can be associated with impacts from flooding or drought, as well as restricting the availability of water (Caretta *et al* 2023). Changes in atmospheric circulation from year to year (including El Niño Southern Oscillation variability) or in response to climate change affect the frequency and intensity of regional extremes. However, amplified seasonality in P−E will continue to intensify the subseasonal and interannual variability in water availability and increase the severity of flooding and drought events where and when they occur as climate continues to warm due to greenhouse gas emissions from human activities.

The magnitude of global changes in P−E maximum and minimum of around 3%–4% per °C of global warming are, however, lower than the rate of low-altitude saturation water vapour pressure increases of about 6–7%/°C dictated by the Clausius Clapeyron equation but greater than the expected global increase in precipitation with warming of around 2–3%/°C (Allan *et al* 2020). A consistent magnitude increase in the global ensemble mean P−E seasonal range of 3.7%/°C is also computed, based on tables 1 and 2: P−E maximum minus minimum increases from 4.48 mm d^{-1} for the present day to 4.86 mm d^{-1} by 2080–2099, an increase of 8.4% for a 2.3 °C global warming. An amplified seasonal range in P−E that is less than the thermodynamic increase in water vapor is to be expected since at the monthly scale, a mix of meteorological conditions can be experienced, associated with convergent and divergent moisture fluxes. Additionally, a weakening of tropical circulation, in part explained by the interaction of energy and moisture balances achieved by the climate system, acts to suppress moisture transport from net evaporative regions into storm systems and monsoons (Allan 2012, Chadwick *et al* 2013). However, projected increases in P−E seasonal range greater than 20% (around 9%/°C global warming) have been identified for some regions, including northern Eurasia and northern North America as well as the equatorial Pacific.

Daily characteristics of precipitation and soil moisture, including their seasonal accumulation, are also important in driving changes in hydroclimatology and water availability (Wainwright *et al* 2022, Ficklin *et al* 2022, Slette *et al* 2022, Duan *et al* 2023, Zaitchik *et al* 2023) but are beyond the scope of the present study. It would also be valuable to further evaluate high-resolution and convection-permitting models since a more realistic frequency and intensity distribution of precipitation may improve the partitioning of precipitation between runoff and storage as well as seasonal P−E and its future projections.

Finally, it is a priority to understand diversity across models and their realism in projecting hydroclimatic response to global warming, including land–sea warming contrast, relative humidity decline, vegetation response to warming and land use change, stomatal response to elevated CO_2 (Berg *et al* 2016, Dunn *et al* 2017, Byrne and O'Gorman 2018, Douville *et al* 2020, Liu *et al* 2023), and robust responses in atmospheric circulation to global warming and its spatial pattern (Byrne *et al* 2018, Watt-Meyer *et al* 2019, Grise and Davis 2020, Su *et al* 2020, Zhao *et al* 2020, Mamalakis *et al* 2021). One additional possibility is to seek relationships between observable responses in P−E seasonality to interannual variability and corresponding changes simulated in future projections (or emergent constraints), with a focus on land where the impacts of water availability acutely influence human societies and the ecosystems upon which they depend.

Data availability statement

The climate model data that support the findings of this study are openly available at the following URL/DOI: https://esgf-node.llnl.gov.

Acknowledgments

This work was funded by the National Center for Earth Observation Grant Number: NE/RO16518/1 and the RCUK grant NE/T001216/1. ERA5 data (Hersbach *et al* 2020) was extracted from https://cds.climate.copernicus.eu/, downloaded version July 2022; CMIP6 climate model datasets (Eyring *et al* 2016) were extracted from https://esgf-node.llnl.gov/search/cmip6/; GPCC data was accessed from http://gpcc.dwd.de and GPCP data downloaded from https://disc.gsfc.nasa.gov/datasets/GPCPMON_3.2. Data was processed using Climate Data Operators (cdo) software (version 1.9.5; Schulzweida 2022) with additional processing using IDL software developed and maintained by Jonathan Gregory and the Met Office. I thank Ingo Richter and an anonymous reviewer for their time in assessing the manuscript and providing valuable suggestions for improvements. Thanks also to the Department of Meteorology Tropical Group at the University of Reading for valuable suggestions.

ORCID iD

Richard P Allan https://orcid.org/0000-0003-0264-9447

References

Alexander J D, McCafferty M K, Fricker G A and James J J 2023 Climate seasonality and extremes influence net primary productivity across California's grasslands, shrublands and woodlands *Environ. Res. Lett.* **18** 064021

Allan R P 2012 Regime dependent changes in global precipitation *Clim. Dyn.* **39** 827–40

Allan R P *et al* 2020 Advances in understanding large-scale responses of the water cycle to climate change *Ann. New York Acad. Sci.* **1472** 49–75

Allan R P, Willett K M, John V O and Trent T 2022 Global changes in water vapor 1979-2020 *J. Geophys. Res.: Atmos.* **127** e2022JD036728

Andrews M B *et al* 2020 Historical simulations with HadGEM3-GC3.1 for CMIP6 *J. Adv. Model. Earth Syst.* **12** e2019MS001995

Andrews T *et al* 2022 On the effect of historical SST patterns on radiative feedback *J. Geophys. Res.: Atmos.* **127** e2022JD036675

Becker A, Finger P, Meyer-Christoffer A, Rudolf B, Schamm K, Schneider U and Ziese M 2013 A description of the global land-surface precipitation data products of the global precipitation climatology centre with sample applications including centennial (trend) analysis from 1901-present *Earth Syst. Sci. Data* **5** 71–99

Berg A *et al* 2016 Land-atmosphere feedbacks amplify aridity increase over land under global warming *Nat. Clim. Change* **6** 869–74

Black E 2023 Global change in agricultural flash drought over the 21st century *Adv. Atmos. Sci.* **40**

Blunden J and Arndt D S 2016 State of the climate in 2015 *Bull. Am. Meteorol. Soc.* **97** Si–S275

Boening C, Willis J K, Landerer F W, Nerem R S and Fasullo J 2012 The 2011 La niña: so strong, the oceans fell *Geophys. Res. Lett.* **39** L19602

Boucher O *et al* 2020 Presentation and evaluation of the IPSL-CM6A-LR climate model *J. Adv. Model. Earth Syst.* **12** e2019MS002010

Byrne M P and O'Gorman P A 2015 The response of precipitation minus evapotranspiration to climate warming: why the 'wet-get-wetter, dry-get-drier' scaling does not hold over land *J. Clim.* **28** 8078–92

Byrne M P and O'Gorman P A 2016 Understanding decreases in land relative humidity with global warming: conceptual model and GCM simulations *J. Clim.* **29** 9045–61

Byrne M P and O'Gorman P A 2018 Trends in continental temperature and humidity directly linked to ocean warming *Proc. Natl Acad. Sci. USA* **115** 4863–8

Byrne M P, Pendergrass A G, Rapp A D and Wodzicki K R 2018 Response of the intertropical convergence zone to climate change: location, width and strength *Curr. Clim. Change Rep.* **4** 355–70

Caretta M *et al* 2023 Water *Climate Change 2022 - Impacts, Adaptation and Vulnerability* (Cambridge University Press) pp 551–712

Chadwick R, Boutle I and Martin G 2013 Spatial patterns of precipitation change in CMIP5: why the rich do not get richer in the tropics *J. Clim.* **26** 3803–22

Chen D, Norris J, Thackeray C and Hall A 2022 Increasing precipitation whiplash in climate change hotspots *Environ. Res. Lett.* **17** 124011

Chen H and Wang S 2022 Accelerated transition between dry and wet periods in a warming climate *Geophys. Res. Lett.* **49** e2022GL099766

Chou C, Chiang J C, Lan C-W, Chung C-H, Liao Y-C and Lee C-J 2013 Increase in the range between wet and dry season precipitation *Nat. Geosci.* **6** 263–7

Dong B and Sutton R 2015 Dominant role of greenhouse-gas forcing in the recovery of Sahel rainfall *Nat. Clim. Change* **5** 757–60

Dong Y, Armour K C, Proistosescu C, Andrews T, Battisti D S, Forster P M, Paynter D, Smith C J and Shiogama H 2021 Biased estimates of equilibrium climate sensitivity and transient climate response derived from historical CMIP6 simulations *Geophys. Res. Lett.* **48** e2021GL095778

Douville H, Allan R P, Arias P A, Betts R A, Caretta M A, Cherchi A, Mukherji A, Raghavan K and Renwick J 2022 Water remains a blind spot in climate change policies *PLOS Water* **1** e0000058

Douville H, Decharme B, Delire C, Colin J, Joetzjer E, Roehrig R, Saint-Martin D, Oudar T, Stchepounoff R and Voldoire A 2020 Drivers of the enhanced decline of land near-surface relative humidity to abrupt 4xCO_2 in CNRM-CM6-1 *Clim. Dyn.* **55** 1613–29

Douville H *et al* 2021 Water Cycle Changes *Contribution of Working Group I. to the Sixth Assessment Report of the Intergovernmental Panel on Climate Change* (*Climate Change 2021: The Physical Science Basis. Contribution of Working Group I to the Sixth Assessment Report of the Ipcc*) ed V Masson-Delmotte, P Zhai, A Pirani, S L Connors, C Péan, S Berger, N Caud, Y Chen, L Goldfarb and M I Gomis (Cambridge University Press) pp 1055–210

Duan S Q, Findell K L and Fueglistaler S A 2023 Coherent mechanistic patterns of tropical land hydroclimate changes *Geophys. Res. Lett.* **50** e2022GL102285

Dunn R J, Willett K M, Ciavarella A and Stott P A 2017 Comparison of land surface humidity between observations and CMIP5 models *Earth Syst. Dyn.* **8** 719–47

Eyring V, Bony S, Meehl G A, Senior C A, Stevens B, Stouffer R J and Taylor K E 2016 Overview of the coupled model intercomparison project phase 6 (CMIP6) experimental design and organization *Geosci. Model. Dev.* **9** 1937–58

Ficklin D L, Null S E, Abatzoglou J T, Novick K A and Myers D T 2022 Hydrological intensification will increase the complexity of water resource management *Earth's Future* **10** e2021EF002487

Fowler H J *et al* 2021 Anthropogenic intensification of short-duration rainfall extremes *Nat. Rev. Earth Environ.* **2** 107–22

Gettelman A *et al* 2019 High climate sensitivity in the community earth system model version 2 (CESM2) *Geophys. Res. Lett.* **46** 8329–37

Gimeno L, Nieto R and Sorí R 2020 The growing importance of oceanic moisture sources for continental precipitation *npj Clim. Atmos. Sci.* **3** 27

Greve P, Orlowsky B, Mueller B, Sheffield J, Reichstein M and Seneviratne S I 2014 Global assessment of trends in wetting and drying over land *Nat. Geosci.* **7** 716–21

Greve P and Seneviratne S I 2015 Assessment of future changes in water availability and aridity *Geophys. Res. Lett.* **42** 5493–9

Grise K M and Davis S M 2020 Hadley cell expansion in CMIP6 models *Atmos. Chem. Phys.* **20** 5249–68

Hausfather Z and Peters G P 2020 Emissions - 'the business as usual' story is misleading *Nature* **577** 618–20

Held I M and Soden B J 2006 Robust responses of the hydrological cycle to global warming *J. Clim.* **19** 5686–99

Hersbach H *et al* 2020 The ERA5 global reanalysis *Q. J. R. Meteorol. Soc.* **146** 1999–2049

Hirasawa H, Kushner P J, Sigmond M, Fyfe J and Deser C 2022 Evolving Sahel rainfall response to anthropogenic aerosols driven by shifting regional oceanic and emission influences *J. Clim.* **35** 3181–93

Huffman G J 2021 GPCP precipitation level 3 monthly 0.5-degree V3.2 (available at: https://disc.gsfc.nasa.gov/datacollection/GPCPMON_3.2.html)

Kumar S, Allan R P, Zwiers F, Lawrence D M and Dirmeyer P A 2015 Revisiting trends in wetness and dryness in the presence of internal climate variability and water limitations over land *Geophys. Res. Lett.* **42** 10867–75

Liepert B G and Previdi M 2012 Inter-model variability and biases of the global water cycle in CMIP3 coupled climate models *Environ. Res. Lett.* **7** 014006

Liu C and Allan R P 2013 Observed and simulated precipitation responses in wet and dry regions 1850–2100 *Environ. Res. Lett.* **8** 034002

Liu L, Ciais P, Wu M, Padrón R S, Friedlingstein P, Schwaab J, Gudmundsson L and Seneviratne S I 2023 Increasingly negative tropical water-interannual CO_2 growth rate coupling *Nature* **618** 755–60

Mamalakis A, Randerson J T, Yu J-Y, Pritchard M S, Magnusdottir G, Smyth P, Levine P A, Yu S and Foufoula-Georgiou E 2021 Zonally contrasting shifts of the tropical rain belt in response to climate change *Nat. Clim. Change* **11** 143–51

Marsh T J, Parry S, Kendon M and Hannaford J A (National Hydrological Monitoring Programme) 2013 *The 2010-12 Drought and Subsequent Extensive Flooding: A Remarkable Hydrological Transformation* (Centre for Ecology and Hydrology)

Milly P C D and Dunne K A 2016 Potential evapotranspiration and continental drying *Nat. Clim. Change* **6** 946–9

Pendergrass A G *et al* 2020 Flash droughts present a new challenge for subseasonal-to-seasonal prediction *Nat. Clim. Change* **10** 191–9

Pendergrass A G, Knutti R, Lehner F, Deser C and Sanderson B M 2017 Precipitation variability increases in a warmer climate *Sci. Rep.* **7** 1–9

Roderick M L, Sun F, Lim W H and Farquhar G D 2014 A general framework for understanding the response of the water cycle to global warming over land and ocean *Hydrol. Earth Syst. Sci.* **18** 1575–89

Samset B H *et al* 2018 Weak hydrological sensitivity to temperature change over land, independent of climate forcing *npj Clim. Atmos. Sci.* **1** 3

Scheff J and Frierson D M W 2015 Terrestrial aridity and its response to greenhouse warming across CMIP5 climate models *J. Clim.* **28** 5583–600

Schmidt G A *et al* 2014 Configuration and assessment of the GISS ModelE2 contributions to the CMIP5 archive *J. Adv. Model. Earth Syst.* **6** 141–84

Schulzweida U 2022 CDO user guide (2.1.0), (Software) (https://doi.org/10.5281/zenodo.5614769)

Schurer A P, Ballinger A P, Friedman A R and Hegerl G C 2020 Human influence strengthens the contrast between tropical wet and dry regions *Environ. Res. Lett.* **15** 104026

Scoccimarro E, Peano D, Gualdi S, Bellucci A, Lovato T, Fogli P G and Navarra A 2022 Extreme events representation in CMCC–CM2 standard and high-resolution general circulation models *Geosci. Model. Dev.* **15** 1841–54

Séférian R *et al* 2019 Evaluation of CNRM Earth system model, CNRM-ESM2-1: role of Earth system processes in present-day and future climate *J. Adv. Model. Earth Syst.* **11** 4182–227

Seland Ø *et al* 2020 Overview of the Norwegian Earth system model (NorESM2) and key climate response of CMIP6 DECK, historical and scenario simulations *Geosci. Model. Dev.* **13** 6165–200

Seneviratne S *et al* 2021 Weather and Climate Extreme Events in a Changing Climate *Working Group I. to the Sixth Assessment Report of the Intergovernmental Panel on Climate Change* (*Climate Change 2021: The Physical Science Basis. Contribution of Working Group I to the Sixth Assessment Report of the Intergovernmental Panel on Climate Change*) ed V Masson-Delmotte *et al* (Cambridge University Press) pp 1513–766

Simmons A J, Willett K M, Jones P D, Thorne P W and Dee D P 2010 Low-frequency variations in surface atmospheric humidity, temperature and precipitation: inferences from reanalyses and monthly gridded observational data sets *J. Geophys. Res.* **115** D01110

Skliris N, Marsh R, Josey S A, Good S A, Liu C and Allan R P 2014 Salinity changes in the World Ocean since 1950 in relation to changing surface freshwater fluxes *Clim. Dyn.* **43** 709–36

Skliris N, Zika J D, Nurser G, Josey S A and Marsh R 2016 Global water cycle amplifying at less than the Clausius-Clapeyron rate *Sci. Rep.* **6** 38752

Slette I J, Blair J M, Fay P A, Smith M D and Knapp A K 2022 Effects of compounded precipitation pattern intensification and drought occur belowground in a mesic grassland *Ecosystems* **25** 1265–78

Song Y H, Nashwan M S, Chung E S and Shahid S 2021 Advances in CMIP6 INM-CM5 over CMIP5 INM-CM4 for precipitation simulation in South Korea *Atmos. Res.* **247** 105261

Su H, Wu L, Zhai C, Jiang J H, Neelin J D and Yung Y L 2020 Observed tightening of tropical ascent in recent decades and linkage to regional precipitation changes *Geophys. Res. Lett.* **47** e2019GL085809

Swaminathan R, Parker R J, Jones C G, Allan R P, Quaife T, Kelley D I, de Mora L and Walton J 2022 The physical climate at global warming thresholds as seen in the U.K. Earth system model *J. Clim.* **35** 29–48

Swart N C *et al* 2019 The Canadian Earth system model version 5 (CanESM5.0.3) *Geosci. Model. Dev.* **12** 4823–73

Tan X, Wu X, Huang Z, Fu J, Tan X, Deng S, Liu Y, Gan T Y and Liu B 2023 Increasing global precipitation whiplash due to anthropogenic greenhouse gas emissions *Nat. Commun.* **14** 2796

Tatebe H *et al* 2019 Description and basic evaluation of simulated mean state, internal variability and climate sensitivity in MIROC6 *Geosci. Model. Dev.* **12** 2727–65

Thomson A M *et al* 2011 RCP4.5: a pathway for stabilization of radiative forcing by 2100 *Clim. Change* **109** 77–94

Vázquez M, Nieto R, Liberato M L and Gimeno L 2022 Influence of teleconnection patterns on global moisture transport during peak precipitation month *Int. J. Climatol.* **43** 932–49

Voldoire A *et al* 2019 Evaluation of CMIP6 DECK experiments with CNRM-CM6-1 *J. Adv. Model. Earth Syst.* **11** 2177–213

Wainwright C M, Finney D L, Kilavi M, Black E and Marsham J H 2021 Extreme rainfall in East Africa, October 2019–January 2020 and context under future *Clim. Change Weather* **76** 26–31

Wainwright C M, Allan R P and Black E 2022 Consistent trends in dry spell length in recent observations and future projections *Geophys. Res. Lett.* **49** e2021GL097231

Watt-Meyer O, Frierson D M and Fu Q 2019 Hemispheric asymmetry of tropical expansion under CO_2 forcing *Geophys. Res. Lett.* **46** 9231–40

Wu T *et al* 2019 The Beijing climate center climate system model (BCC-CSM): the main progress from CMIP5 to CMIP6 *Geosci. Model. Dev.* **12** 1573–600

Wu T *et al* 2020 Beijing climate center Earth system model version 1 (BCC-ESM1): model description and evaluation of aerosol simulations *Geosci. Model. Dev.* **13** 977–1005

Yuan X, Wang Y, Ji P, Wu P, Sheffield J and Otkin J A 2023 A global transition to flash droughts under climate change *Science* **380** 187–91

Yukimoto S *et al* 2019 The meteorological research institute Earth system model version 2.0, MRI-ESM2.0: description and basic evaluation of the physical component *J. Meteorol. Soc. Japan* **97** 931–65

Zaitchik B F, Rodell M, Biasutti M and Seneviratne S I 2023 Wetting and drying trends under climate change *Nat. Water* **1** 502–13

Zhao M *et al* 2018 The GFDL global atmosphere and land model AM4.0/LM4.0: 1. Simulation characteristics with prescribed SSTs *J. Adv. Model. Earth Syst.* **10** 691–734

Zhao X, Allen R J, Wood T and Maycock A C 2020 Tropical belt width proportionately more sensitive to aerosols than greenhouse gases *Geophys. Res. Lett.* **47** e2019GL086425

Ziehn T, Chamberlain M A, Law R M, Lenton A, Bodman R W, Dix M, Stevens L, Wang Y-P and Srbinovsky J 2020 The Australian Earth system model: ACCESS-ESM1.5 *J. South. Hemisphere Earth Syst. Sci.* **70** 193–214